Basset-Boussinesq history force acting on a drop in an oscillatory flow

Hadrien Godé [1,2] Sophie Charton [1] Eric Climent [2] and Dominique Legendre [2,*]

[1]*CEA, DES, ISEC, DMRC, Université Montpellier, Marcoule, France*
[2]*Institut de Mécanique des Fluides de Toulouse (IMFT), UMR 5502, CNRS,*
Université de Toulouse, 31400 Toulouse, France

The total force experienced by a droplet embedded in a uniform oscillating flow can be divided into four contributions: steady drag force, inertial or pressure gradient force, added-mass force, and Basset-Boussinesq history force. The effect of the history force is often neglected, due to numerical difficulties for its time integration, but also because no analytic expression is available in the time domain for droplets. The contribution of the history force acting on a spherical droplet in an oscillatory flow is determined using direct numerical simulation. Variation of the viscosity ratio makes the analysis relevant to bubbles, droplets, and solid particles. By changing the flow oscillation frequency, we can determine the range of physical parameters for which the contribution of the history force is significant. Additionally, the relevance of the kernel expression recently proposed by Legendre *et al.* [Phys. Rev. Fluids **4**, 073603 (2019)] is discussed and compared to theoretical predictions in the frequency domain. We demonstrate that this kernel can be used to model history effects for droplets, especially since the contribution of the history force to the total force is important. The proposed history force expression provides a significant improvement for droplet trajectory prediction when the history force contribution cannot be neglected.

I. INTRODUCTION

Predicting droplet dynamics is of primary importance in many applications related to natural and industrial situations, where different flow conditions and liquid/liquid systems can be encountered. Predicting droplet dynamics is particularly challenging in strongly unsteady situations. In this study, we focus on the history force contribution to the force balance. Depending on the viscosity ratio, the physical configuration may vary from liquid droplets in a gas for cloud microphysics [1], gas bubbles in a liquid as encountered in bubble columns for petrochemical, and chemical industries or liquid-liquid systems related to solvent extraction, petroleum, or other processes involving emulsions.

Under such operating conditions, the flow of the carrier fluid is commonly turbulent, which means that droplets experience a wide range of temporal fluctuations. Modeling approaches based on Euler-Lagrange formalism are well suited to account for the effects of temporal and spatial turbulent structures of the fluid flow on particle trajectories obtained through time integration of the force balance. Analytic formulations of the force balance are built by integrating specific forces: (i) the drag force related to the resistance due to the relative (or slip) velocity between the droplet and the surrounding fluid, (ii) the history force which is a correction to steady drag for fluctuating slip velocities, accounting for the unsteady viscous diffusion of vorticity produced at the interface, (iii) the added mass force that originate from inertial effects due to both the droplet and fluid

---

*legendre@imft.fr

accelerations, (iv) the inertial or pressure gradient force due to the mean flow oscillations, and (v) the lift force induced by the presence of velocity gradients in the flow field whose contribution is orthogonal to the relative motion.

History force has often been neglected because its integration over viscous diffusion times of several order of magnitudes requires tedious algorithms (high computational cost and large memory storage of the relative acceleration). But also because its expression has been an open question for viscous fluid particles. However, recent literature has demonstrated the need to consider this force, as in Refs. [2–4]. The history force has been found to have a significant impact on the particle's slip velocity and acceleration, resulting in modified preferential accumulation and collision rates. It is now possible to consider the history force in CFD because of the continuous increase in computing resources, but also thanks to numerical algorithms dedicated to the temporal integration of the history kernel [5–7]). In addition, a history kernel for the history force has recently been proposed by Legendre *et al.* [8].

In this paper, we study the hydrodynamics of a fluid sphere in a uniform oscillatory flow. We aim at specifying with direct numerical simulations the conditions under which the history force is significant. The impulsive flow conditions studied in Legendre *et al.* [8] are extended to the periodic flow encountered in applications *e.g.,* in oscillatory flow reactors and pulsed columns.

The paper is organized as follows. First, we describe the flow configuration and the numerical methods. Second, we describe the flow structure, both inside and outside the droplet. Then, we discuss the quantitative contribution of the history force to the total momentum balance and conclude on the accuracy of the proposed analytic history force kernel over a wide range of the relevant dimensionless parameters, i.e., the viscosity ratio and the droplet Stokes number.

II. PROBLEM STATEMENT

We consider a fluid sphere of radius R, density ρ_i, and viscosity μ_i moving at a velocity $V(t)$ in an unbounded continuous fluid phase of density ρ_e, viscosity μ_e, and velocity $U(t)$. We define $W(t) = U(t) - V(t)$ as the relative velocity of the fluid with respect to the moving sphere.

Under Stokes flow conditions, the fluid sphere experiences a total force $F(t)$ which breaks down into four contributions: the steady drag force F_{SD} [9,10], the added-mass force F_{AM} [11,12], the inertial or pressure gradient force F_I, and the Basset-Boussinesq history force F_H described in Basset [13] and Boussinesq [14] for a solid sphere, in Mei *et al.* [15], Yang and Leal [16] for spherical bubbles, and recently revisited by Legendre *et al.* [8] for fluid viscous spheres. These contributions write respectively from left to right:

$$F(t) = 6\pi \mu_e R \frac{2 + 3\mu^*}{3 + 3\mu^*} W(t) + C_m \rho_e \frac{4}{3}\pi R^3 \frac{dW}{dt} + \rho_e \frac{4}{3}\pi R^3 \frac{dW}{dt} + 6\pi \mu_e R \int_0^t \frac{dW}{dt'} K_\mu(t - t', \mu^*)\, dt',$$

(1)

where $\mu^* = \mu_i/\mu_e$ is the viscosity ratio, C_m is the added mass coefficient which is equal to $\frac{1}{2}$ for spheres, and K_μ the history force kernel whose expression depends on μ^*. In the following, the added mass force and the inertial (pressure gradient) force are combined into a single term.

Boussinesq [14] and Basset [13] proposed an expression for K_μ for solid particle in the time domain. This kernel is valid for systems with high μ^*, i.e., when the viscosity of the fluid sphere is much higher than that of the surrounding fluid yielding no-slip at the surface:

$$K_\mu(t, \mu^* \to \infty) = \frac{1}{\sqrt{\pi t/t_v}},$$

(2)

where $t_v = R^2/\nu_e$ is the characteristic diffusion time in the surrounding fluid. For a bubble (shear free interface), or when the viscosity of the fluid sphere is much lower than the surrounding fluid,

the kernel writes [16]:

$$K_\mu(t, \mu^* \to 0) = \frac{4}{3} \exp\left[9\frac{t}{t_\nu}\right] \operatorname{erfc}\left[3\sqrt{\frac{t}{t_\nu}}\right]. \tag{3}$$

Considering the transient evolution of a droplet suddenly submitted to a uniform and constant flow under creeping flow conditions, Legendre *et al.* [8] have reported that the slip length along the interface reaches a uniform constant value:

$$\lambda(\mu^*) = \frac{R}{3\mu^*}. \tag{4}$$

Based on this result, the kernel expression determined for a slip sphere [11,17,18],

$$K_\mu(t, \lambda) = \frac{(1 + 2\lambda/R)^2}{\lambda/R(1 + 3\lambda/R)} \exp\left[\frac{(1 + 3\lambda/R)^2}{\lambda^2/R^2} \frac{t}{t_\nu}\right] \operatorname{erfc}\left[\frac{(1 + 3\lambda/R)}{\lambda/R} \sqrt{\frac{t}{t_\nu}}\right], \tag{5}$$

has been extended to the case of droplet with a finite viscosity ratio μ^* as

$$K_\mu(t, \mu^*) = \frac{(2 + 3\mu^*)^2}{3(1 + \mu^*)} \exp\left[9(1 + \mu^*)^2\frac{t}{t_\nu}\right] \operatorname{erfc}\left[3(1 + \mu^*)\sqrt{\frac{t}{t_\nu}}\right]. \tag{6}$$

This expression has been found to properly reproduce direct numerical simulations of a fluid sphere in an impulsive uniform flow. The accuracy of this analytic kernel for an oscillating creeping flow is investigated here by considering the unsteady periodic flow,

$$W(t) = W_0[1 + \sin(2\pi f t)], \tag{7}$$

where f is the oscillation frequency.

For such an oscillating flow, an exact solution of the total force 1 can be expressed in the frequency domain considering the solution derived by Gorodtsov [19]. Yang and Leal [16] and Kim and Karrila [20] investigated theoretically the motion of viscous spheres. A small error was present in that paper; see the discussion by Pozrikidis [21]. This has been corrected by Galindo and Gerbeth [22]. Following the notation of Abbad and Souhar [23], the corresponding force expression in the frequency domain is

$$\tilde{F}(f^*) = 6\pi\mu_e R\tilde{W}(f^*)\left[\frac{2 + 3\mu^*}{3(1 + \mu^*)} + \frac{K_o^2}{3} + \frac{\mu^*}{1 + \mu^*}K_o + L(K_i, K_o, \mu^*)\right], \tag{8}$$

where $\tilde{W}(f^*)$ is the Fourier transform of the flow oscillation, and $L(K_i, K_o, \mu^*)$, Q, K_o, and K_i are given by

$$L(K_i, K_o, \mu^*) = \frac{1 + 3K_o}{3(1 + \mu^*)} - \frac{(1 + K_o)^2}{3 + K_o + \mu^* Q(k_i)}, \tag{9}$$

$$Q = \frac{K_i(6 + K_i^2) - 3(2 + K_i^2)\tanh(K_i)}{(3 + K_i^2)\tanh(K_i) - 3K_i}, \tag{10}$$

$$K_o = \sqrt{-2\pi i f^*}, \quad K_i = K_o\sqrt{\frac{\rho^*}{\mu^*}}, \tag{11}$$

where i is the complex number. In this work, the oscillation frequency f is normalized by the diffusive time $t_\nu = R^2/\nu_e$ using the kinematic viscosity of the external fluid:

$$f^* = f t_\nu = \frac{fR^2}{\nu_e}. \tag{12}$$

TABLE I. Range of dimensionless parameters (Re, μ^*, ρ^*, f^*) explored in numerical simulations

Re	μ^*	ρ^*	f^*
$[10^{-2}, 10^{-1}]$	$[0.05, 0.2, 5, 20]$	1	$[10^{-3}, 10^{-2}, 10^{-1}, 1, 10, 10^2, 10^3]$

Similarly, the flow frequency can be normalized with the internal diffusion time: $f_i^* = fR^2/\nu_i = f^*\rho^*/\mu^*$. In Eq. (8), the four contributions from left to right are the steady drag force, the added mass force and the inertial (pressure gradient) force combined in a single term, and the two last terms give the history force for viscous spheres as

$$\tilde{F}_H(f^*, \mu^*) = 6\pi\mu_e R\tilde{W}(f^*)\left[\frac{\mu^*}{1+\mu^*}K_o + L(K_i, K_o, \mu^*)\right]. \tag{13}$$

$K_o\mu^*/(1+\mu^*)$ is the extension of the Basset-Boussinesq term K_o to fluid spheres while $L(K_i, K_o, \mu^*)$ is an additional term specific to fluid spheres. The limit $\mu^* \to \infty$ gives the solid sphere behavior (Basset-Boussinesq history force)

$$\tilde{F}_H(f^*, \mu^* \to \infty) = 6\pi\mu_e RK_o\tilde{W}(f^*), \tag{14}$$

while the limit $\mu^* \to 0$ gives the spherical bubble behavior (Yang and Leal history force),

$$\tilde{F}_H(f^*, \mu^* = 0) = 8\pi\mu_e R\frac{K_o}{3+K_o}\tilde{W}(f^*). \tag{15}$$

As shown by relation (14), for a solid sphere $\tilde{F}_H(f^*, \mu^* \to \infty) \sim \sqrt{f^*}\tilde{W}(f^*)$ for all frequencies, while from relation (15) for a spherical bubble $\tilde{F}_H(f^*, \mu^* = 0) \sim \sqrt{f^*}\tilde{W}(f^*)$ at low frequency and is independent on the frequency at high frequency. The Eqs. (13)–(15) will be used for a direct comparison with our numerical simulations and to discuss the relevance of the kernel proposed in this study for fluid spheres.

Under the flow conditions considered in this paper, the flow field around a fixed fluid sphere is *a priori* controlled by four dimensionless numbers: the droplet Reynolds number Re based on the physical properties of the external fluid, the viscosity ratio μ^*, the density ratio ρ^*, respectively, defined as

$$\text{Re} = \frac{2R\rho_e W_0}{\mu_e}, \quad \mu^* = \frac{\mu_i}{\mu_e}, \quad \rho^* = \frac{\rho_i}{\rho_e}, \tag{16}$$

and the normalized oscillation frequency f^*. For low values of both f^* and f_i^*, momentum diffusion dominates both inside and outside the droplet. The local velocity field is hence expected to quickly adjust to the flow oscillations with a quasistatic evolution corresponding to a weak history force contribution. For large values of f^* or f_i^* important delays in diffusion are expected, yielding a significant contribution of the history force on the momentum balance.

In the following, we report on an extensive analysis of the quantitative contribution of the history force both in the frequency and time domains by varying the viscosity ratio μ^* and the normalized frequency f^* considering Reynolds number much smaller than 1. To reduce the range of parameters explored, the density ratio ρ^* is set to 1, as it has been shown to have little influence on the history force [24,25]. The parametric study was carried out within the range of parameters reported in Table I.

III. NUMERICAL METHOD

The simulations were carried out using the JADIM code developed at IMFT. This code, initially dedicatd to the direct simulation of unsteady 3D flows around solid spheres and spherical bubbles [26,27] has recently been extended to study the flow dynamics related to fluid spheres [8,25,28].
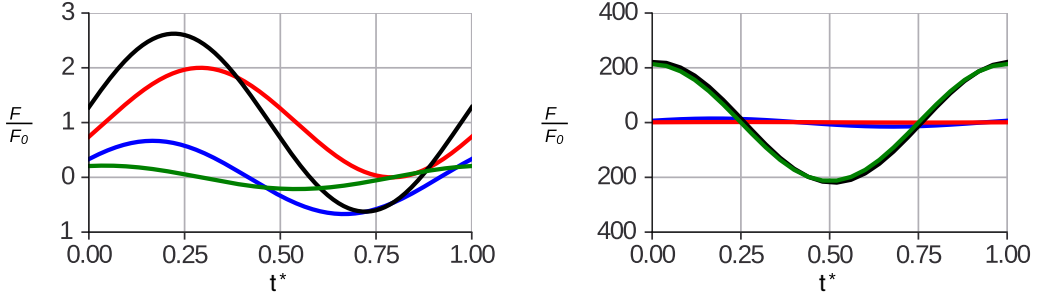
FIG. 1. Time evolution of the forces acting on a droplet over one period of a uniform oscillatory flow ($t^* = tf$): —— Total force, —— Steady drag force F_{SD}, —— Inertial and added-mass force $F_{I\&AM}$, —— History force F_H. (Left) Re = 0.01, $\mu^* = 5$ and $f^* = 0.1$ ($f_i^* = 0.02$). (Right) Re = 0.1, $\mu^* = 5$, and $f^* = 100$ ($f_i^* = 20$). All forces are scaled by the mean steady drag force over the period F_0 given by Eq. (20).

We refer the reader to these references for a detailed presentation of the code, as well as its validation for the simulation of such problems. In this study, an axisymmetric polar mesh is used to solve the flow both inside and outside the droplet, with typically hundreds of cells regularly distributed along the interface. The droplet is set fixed at the origin of a domain extending from $x = -50R$ to $x = 50R$, to reduce confinement effect for the considered range of Reynolds number. The Navier-Stokes equations are integrated in space using a finite volume method using a second order centered scheme, while time advancement is achieved through a three steps Runge-Kutta scheme (the nonlinear terms are computed explicitly while the diffusive terms are computed using a Crank-Nicolson scheme). The time step was chosen to satisfy both the CFL stability criterion of the numerical method and to guarantee a minimum of 100 time steps per flow oscillation period ($1/f$). The simulations are conducted by first simulating the steady flow induced by a constant inlet velocity W_0. Once a steady state is reached, the periodic flow given by Eq. (7) is imposed as a boundary condition at the domain inlet (at $x = -50R$). Then we let the simulation run over several characteristic times t_v to reach the periodic oscillating solution.

The unsteady total force $F(t)$ acting on the droplet is calculated by the direct integration of the pressure and viscous stresses over the interface separating the two fluids. The force decomposition into the steady drag, the added-mass force and the Basset-Boussinesq history force is described below. Considering the analytic expressions of both the steady drag force:

$$F_{\text{SD}}(t) = 6\pi\mu_e R\frac{2 + 3\mu^*}{3 + 3\mu^*}W_0[1 + \sin(2\pi ft)], \tag{17}$$

and the sum of the inertial (pressure gradient) force and the added-mass force:

$$F_{\text{SD}}(t) = 4\pi^2\rho_e R^3 fW_0\cos(2\pi ft), \tag{18}$$

the history force is determined as

$$F_{\text{H}}(t) = F(t) - F_{\text{SD}}(t) - F_{I\&AM}(t). \tag{19}$$

Figure 1 compares the magnitude of these forces over a period of the oscillating flow for two specific cases: Re = 0.01, $\mu^* = 5$, $f^* = 0.1$ ($f_i^* = 0.02$), and Re = 0.1, $\mu^* = 5$, $f^* = 100$ ($f_i^* = 20$). All forces are scaled by the mean steady drag force over the period:

$$F_0 = 6\pi\mu_e RW_0\frac{2 + 3\mu^*}{3 + 3\mu^*}. \tag{20}$$

Each contribution follows a periodic oscillation due to the sinusoidal velocity forcing. When the fully periodic regime is reached, each force can be decomposed into an average and a fluctuating

part as

$$F(t) = \overline{F} + F'(t), \tag{21}$$

with $\overline{F}$ the mean value of F and $F'(t)$ the unsteady fluctuation over an oscillation period. This enables to characterize the intensity of the unsteady contribution $F'(t)$ using the Root-Mean-Square (RMS) metrics, defined as

$$\text{RMS}(F) = \sqrt{\frac{1}{n} \sum_{i=1}^{n} (F'(i))^2}, \tag{22}$$

where n is the number of time steps over the considered period.

IV. FLOW FIELD DESCRIPTION

The streamlines inside and around the droplet are reported in Fig. 2 at different times of the oscillation period, in the case Re = 0.1, $\mu^* = 0.2$, and $f^* = 1$. In this configuration, the external fluid is more viscous than the fluid inside the droplet. Over the time period, the structure of the flow has been observed to evolve drastically over the time period. In particular, counterrotating vortices appear both inside and outside the droplet.

At the beginning of the oscillation period [Fig. 2(a)], the streamlines are similar to the streamlines of a steady uniform Stokes flow around a viscous drop: a Hill's spherical vortex turns clockwise inside the drop entrained by the viscous stress at the interface exerted by the external flow moving from left to right. Linearity of Stokes equations yields fore-aft symmetry of the creeping flow streamlines.

This streamlines structure is observed until the inlet velocity reaches its maximum $W(t) = 2 W_0$ at $t = T/4$ [Fig. 2(b)], and also when it decelerates down to $W(t) = W_0$ at $t = T/2$. Just after the half period at time $t = 0.554T$ when $W(t) = 0.667 W_0$, Fig. 2(d) shows the appearance of a small recirculation zone located in the near wake of the drop.

Under oscillating flow conditions around a solid sphere at Reynolds varying from 0.1 to 40, similar phenomena have already been observed during the phase of the flow deceleration [6,29]. The flow separation has been observed in the decelerating phase of the oscillation: under strong decelerating conditions the flow can completely detach itself from the sphere and a reverse flow surrounds the sphere.

Then, this recirculation region grows along the upstream direction, its size increases and finally completely covers the drop [Fig. 2(e)]. Meanwhile, a second vortex develops inside the drop to match this clockwise external recirculation with the internal flow, while the size of the external vortex increases along the radial direction [Fig. 2(f)].

The second internal recirculation vortex increases from $t = 0.582 T$ to $t = 0.8 T$ [Fig. 2(h)], while the first one vanishes, resulting in a Hill spherical vortex now rotating counterclockwise. At $t = 0.883 T$, a new recirculation appears close to the front stagnation point [Fig. 2(i)], and develops between the drop and the clockwise oriented external recirculation, which eventually vanishes at the end of the period.

The evolution of the tangential velocity U_θ along the drop interface, normalized by W_0 is reported in Fig. 3 at the same times as in Fig. 2. We can observe that the sign of U_θ is changing during the period, between $t = 0.582 T$ and $t = 0.8 T$, in agreement with the development of the external clockwise and internal counterclockwise vortices. The evolution of the longitudinal velocity $U_x(x = 0, r)$ is reported as a function of the radial distance r to the symmetry axis. Due to the development of the two vortices, the direction of U_x changes considerably over the period. The affected region extends for a distance of about $3R$ around the drop interface. Beyond this region, the flow direction is controlled by the upstream velocity $W(t)$ prevailing far from the drop.

The influence of the viscosity ratio on the flow structure is illustrated in Fig. 4 for Re = 0.1, $\mu^* = 5$, and $f^* = 1$. The viscosity ratio is the inverse of that considered in Fig. 2 which means that the

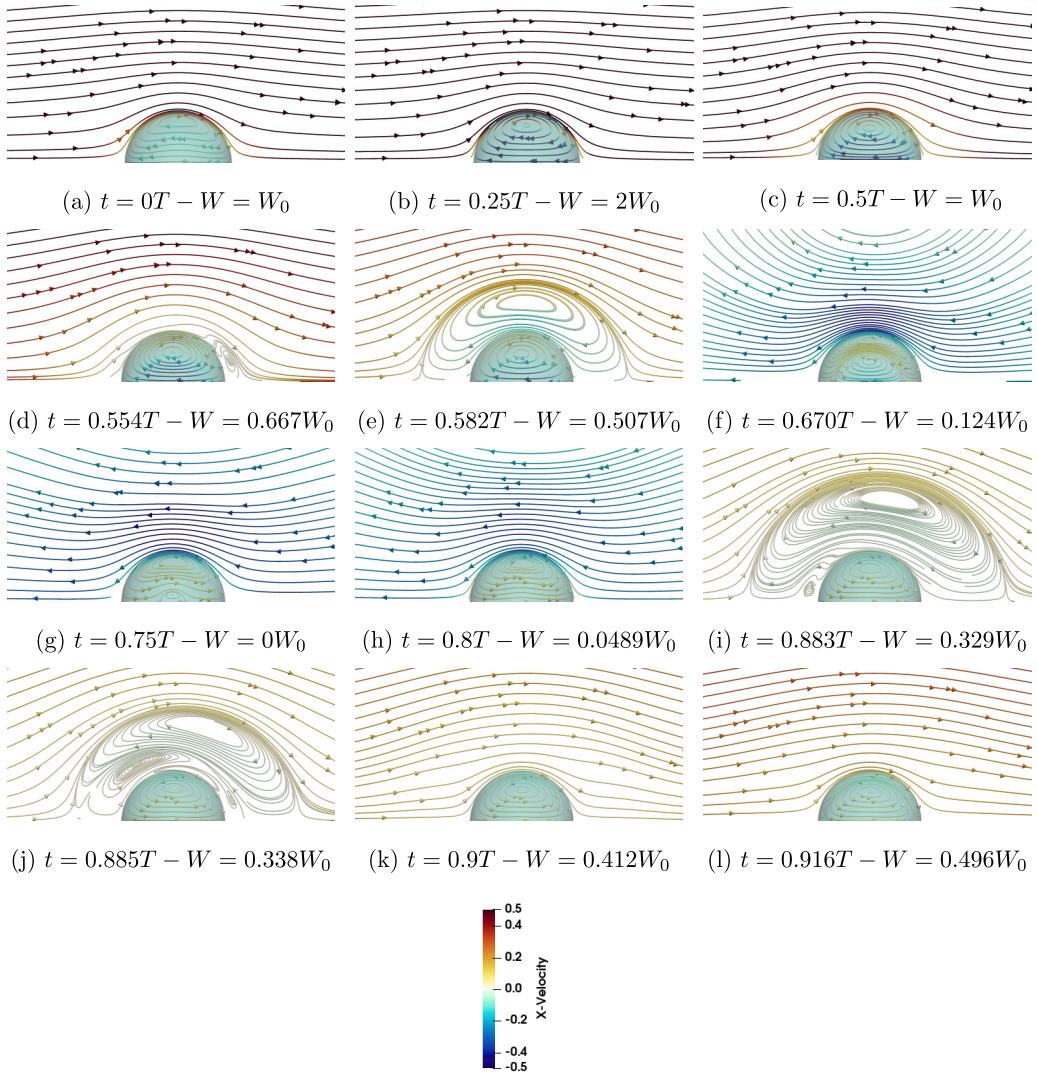FIG. 2. Visualization of the streamlines inside and around a viscous droplet at different times of the oscillation period, for Re = 0.1, $\mu^* = 0.2$, and $f^* = 1$. More instants are shown during the second half of the period to provide a detailed description of the two recirculation vortices that develop both inside and outside the drop during the deceleration phase. From (a) to (l) increasing time over a period. The time t and the corresponding velocity W are given under each figure.

external fluid is now less viscous than the fluid inside the droplet. A flow structure similar to Fig. 2 is observed over the period, with the development of external clockwise and internal counterclockwise vortices. However, recirculations appear earlier and grow faster for $\mu^* = 5$. One explanation is that the presence of a more viscous liquid inside the drop causes the continuous phase motion to remain controlled by the inner fluid motion as a consequence of the continuity of the tangential velocity at the droplet interface.

To consider now the effect of the oscillation frequency, Figs. 5 and 6 compare the streamlines obtained inside and around the drop at $f^* = 10^{-2}$ and $f^* = 10^3$, respectively. The Reynolds number and viscosity ratio are the same as in Fig. 2 (Re = 0.1 and $\mu^* = 0.2$). A significant effect of f^*
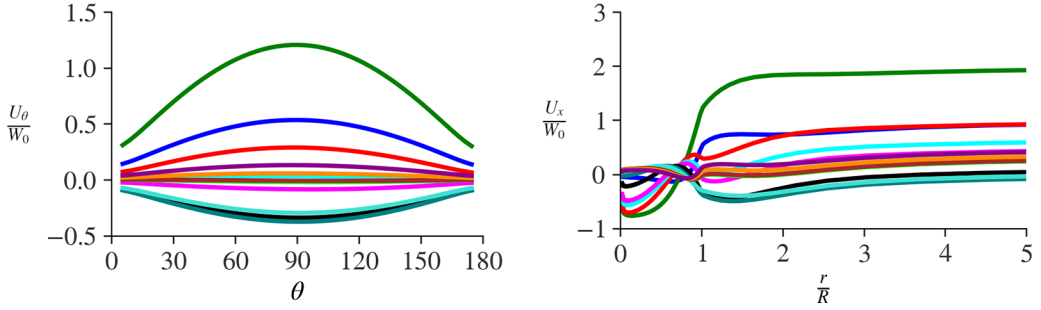
FIG. 3. (Left) Evolution of the normalized tangential velocity U_θ/W_0 with the polar angle θ at the interface. (Right) Radial evolution of the normalized axial velocity $U_x(x = 0, r)/W_0$. The times considered are the same as in Fig. 2: ____ $t = 0T$, $W(t) = W_0$ [Fig. 2(a)], ____ $t = 0.554T$, $W(t) = 0.667W_0$ [Fig. 2(b)], ____ $t = 0.582T$, $W(t) = 0.507W_0$ [Fig. 2(c)], ____ $t = 0.670T$, $W(t) = 0.124W_0$ [Fig. 2(d)], ____ $t = 0.800T$, $W(t) = 0.0489W_0$ [Fig. 2(e)], ____ $t = 0.883T$, $W(t) = 0.329W_0$ [Fig. 2(f)].

can be observed on the development of the flow. For $f^* = 10^{-2}$, a quasistatic evolution of the flow was expected, with a flow field corresponding at each time to that of a drop under steady condition. However, the external vortices are still observed, revealing a strong coupling between the flow oscillation and the flow field response. An evolution similar to the one reported for $f^* = 1$ is observed, with the development of two vortices inside and outside the drop, but over a shorter part of the period (Fig. 5). For $f^* = 10^3$ the flow structure around and inside the drop cannot follow the fast dynamics of the external flow. This is observed in Fig. 7 where the radial profile of the external flow shows no change inside the drop. The transition from external to internal flow occurs across a very thin diffusion layer. However, the development of two vortices is still observed in the outer region, as shown in Fig. 6(e).
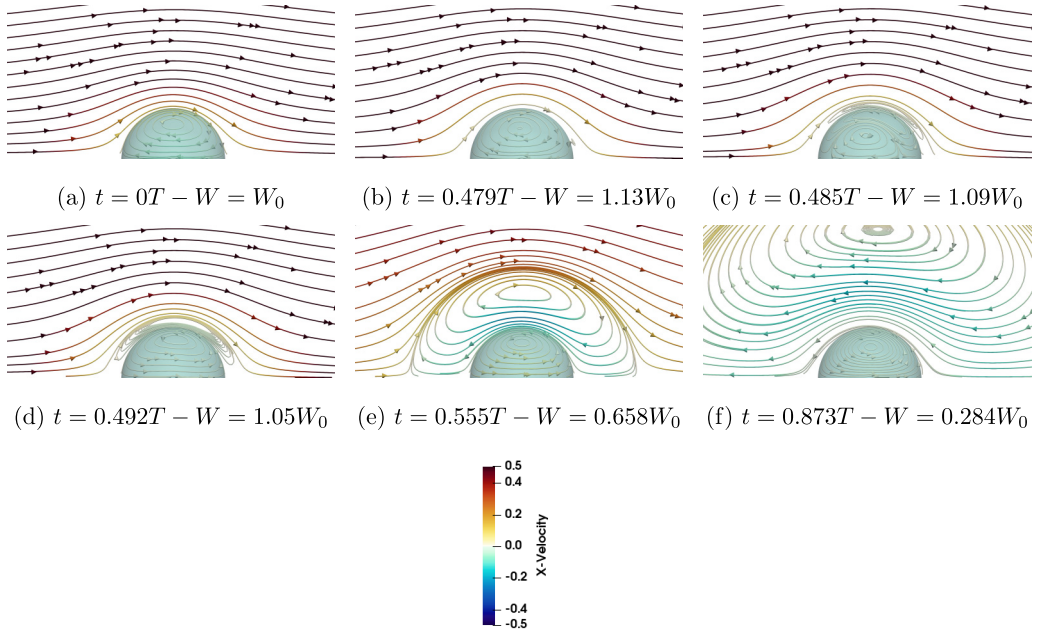

(a) $t = 0T - W = W_0$ (b) $t = 0.479T - W = 1.13W_0$ (c) $t = 0.485T - W = 1.09W_0$

(d) $t = 0.492T - W = 1.05W_0$ (e) $t = 0.555T - W = 0.658W_0$ (f) $t = 0.873T - W = 0.284W_0$

FIG. 4. Visualization of the streamlines over the oscillation period for Re $= 0.1$, $\mu^* = 5$, and $f^* = 1$. From (a) to (f) increasing time over a period. The time t and the corresponding velocity W are given under each figure.
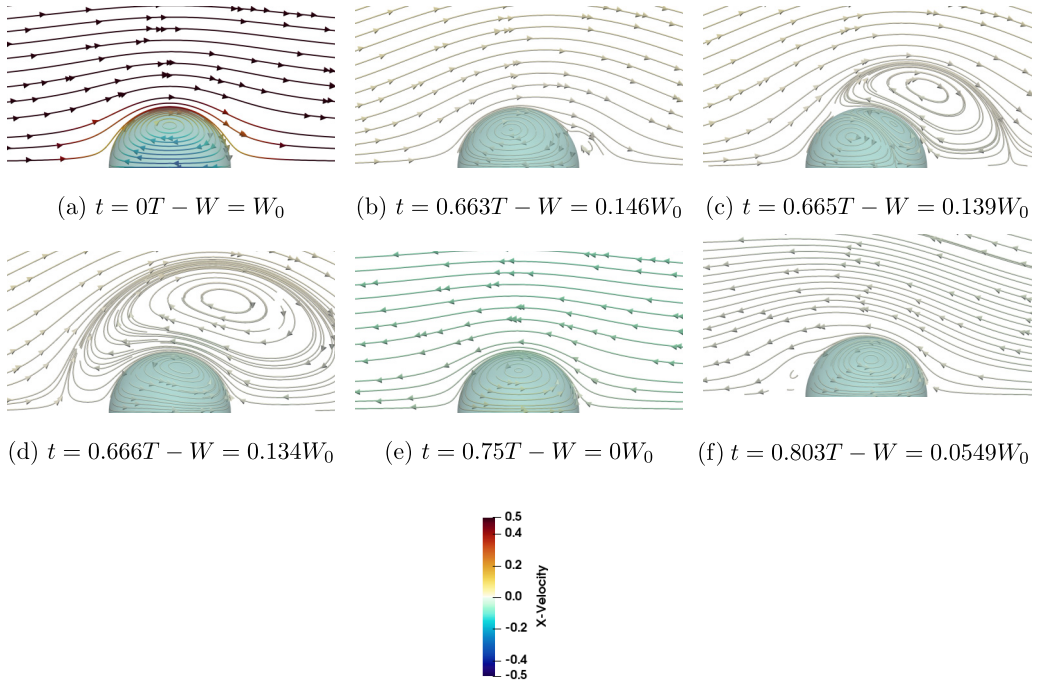
(a) $t = 0T - W = W_0$

(b) $t = 0.663T - W = 0.146W_0$

(c) $t = 0.665T - W = 0.139W_0$

(d) $t = 0.666T - W = 0.134W_0$

(e) $t = 0.75T - W = 0W_0$

(f) $t = 0.803T - W = 0.0549W_0$

FIG. 5. Visualization of the streamlines over one period for Re $= 0.1$, $\mu^* = 0.2$, and $f^* = 0.01$. From (a) to (f) increasing time over a period. The time t and the corresponding velocity W are given under each figure.
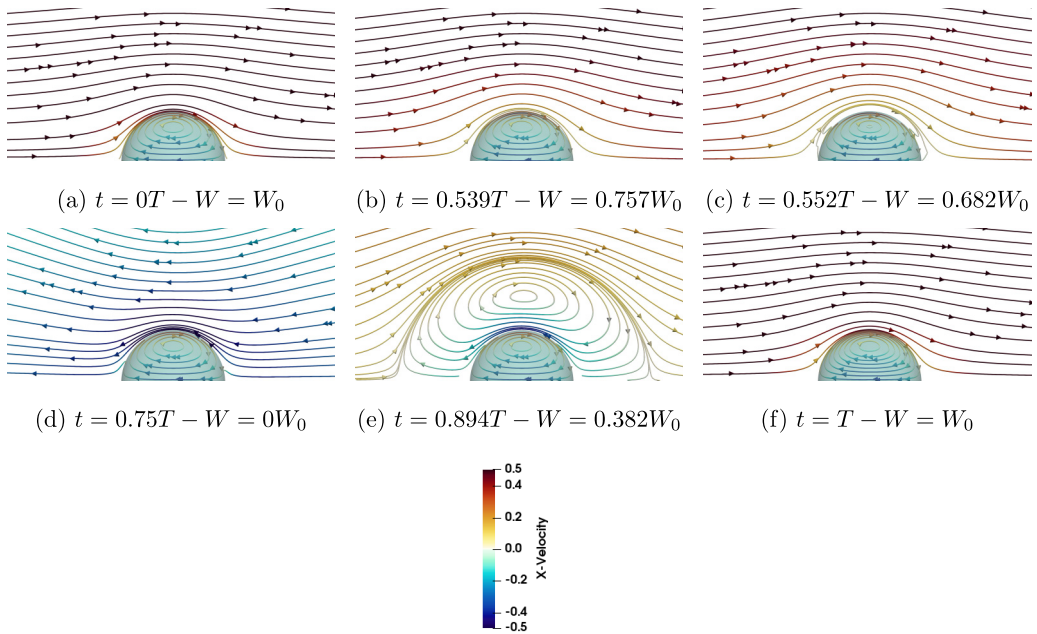

(a) $t = 0T - W = W_0$

(b) $t = 0.539T - W = 0.757W_0$

(c) $t = 0.552T - W = 0.682W_0$

(d) $t = 0.75T - W = 0W_0$

(e) $t = 0.894T - W = 0.382W_0$

(f) $t = T - W = W_0$

FIG. 6. Visualization of the streamlines over one period for Re $= 0.1$, $\mu^* = 0.2$, and $f^* = 10^3$. From (a) to (f) increasing time over a period. The time t and the corresponding velocity W are given under each figure.
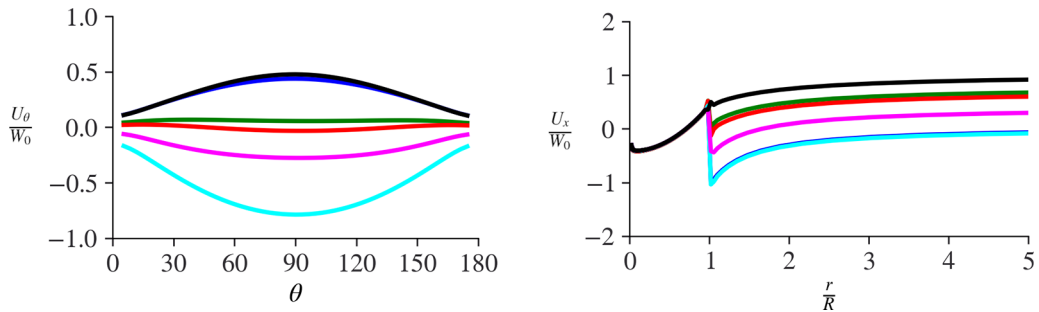
FIG. 7. (Left) Evolution of the normalized tangential velocity U_θ/W_0 as a function of the polar angle θ at the interface. (Right) Radial evolution of the normalized axial velocity $U_x(x=0,r)/W_0$. The times considered are the same as in Fig. 6: ⸺ Fig. 6(a), ⸺ Fig. 6(b), ⸺ Fig. 6(c), ⸺ Fig. 6(d), ⸺ Fig. 6(e), ⸺ Fig. 6(f).

The fraction of the period during which the external recirculation is observed is a relevant indicator to quantify the impact of the oscillation on the flow field change. When the imposed velocity oscillates at moderate frequency, $f^* = 1$, the external recirculation is observed during 43% of the period duration. When reducing the frequency, the flow seems to evolve toward a mostly quasistatic pattern, a recirculation being observed during 13% of the period duration for $f^* = 0.01$. At last, in the case of high-frequency fluctuations, $f^* = 10^3$, the recirculation is observed up to 50% of the period.

V. DISCUSSION ON FORCE CONTRIBUTIONS

We now consider the force decomposition as introduced in the section Numerical method. Due to the flow reversibility and to the linearity of Stokes equations, the mean history force (17) is zero. At low Re, there is no coupling between the effects of the steady component of the flow and its unsteady periodic oscillation. Therefore, in the fully periodic regime, the average total force is equal to the steady drag force F_0 corresponding to the mean flow W_0. From the analytical expression of the pressure gradient and added-mass force, it is obvious that the time average of this force is zero as well, such that the mean contributions of the force are

$$\overline{F_{\text{tot}}} = \overline{F_{\text{SD}}} = 6\pi\mu_e R W_0 \frac{2+3\mu^*}{3+3\mu^*}, \quad \overline{F_{\text{I\&AM}}} = 0, \quad \overline{F_H} = 0. \tag{23}$$

According to our simulations, these conditions are satisfied, the measured values of $\overline{F_{\text{I\&AM}}}$ and $\overline{F_H}$ being both lower than $3 \times 10^{-3} F_0$.

To compare the relative contributions of each force, we consider their RMS magnitude over one oscillation period. For given Reynolds number and viscosity ratio, the RMS values of the history force, inertial and added-mass force and therefore the total force amplitude depend on f^* while the RMS of the drag force has a constant value because it does not depend on the oscillation frequency f. The results are shown in Fig. 8, where we use the mean value of the steady drag force F_0 to scale all the RMS contributions.

The history force RMS is observed to increase with f^* and to become larger than the steady drag force for $f^* \geqslant 1$. The inertial (pressure gradient) and added-mass forces RMS are also increasing with f^* but with a faster rate so that it controls the total force magnitude for $f^* > 30$. As a consequence, the fluctuating contributions of both the steady drag and history forces can be neglected at large frequencies. Indeed, it is possible to make the forces dimensionless using $6\pi\mu_e R W_0$ and time using f^{-1} in equation (1). Therefore, the drag force becomes of order unity and the added mass force and pressure gradient term scale with f^* dominating the total force for rapid oscillating flows. Depending on the asymptotic behavior of the kernel at high frequency the history
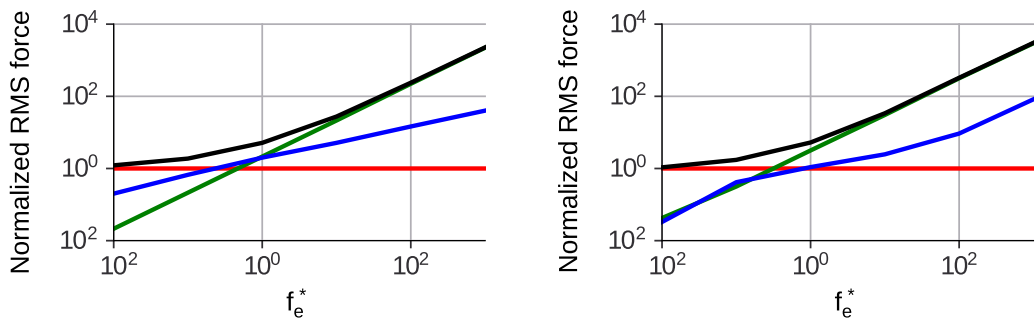
FIG. 8. Evolution of all RMS contributions normalized by F_0 as a function of f^*. —— Total force RMS, —— Steady force RMS, —— Inertial (Pressure gradient) and Added-mass forces RMS, —— History force RMS. (Left) Simulation results for Re $= 0.01$ and $\mu^* = 20$. (Right) Simulation results for Re $= 0.1$ and $\mu^* = 0.05$.

force scales differently. For solid particles, the Basset history force scales with $(f^*)^{1/2}$ whereas it becomes constant for bubbles. For droplets with finite viscosity ratio, the high frequency regime evolves between these two limits.

To gain a quantitative analysis of the history force contribution to the total force balance, we seek the conditions yielding the history force RMS to be more than 10% of the total force RMS. To do so, we plot the relative contribution (to the total force RMS) of each force RMS in Fig. 9 as a function of f^*. As observed in the figure, the oscillating contribution of the history force appears to be significant when $0.01 \leqslant f^* \leqslant 10$.

VI. HISTORY FORCE IN THE FREQUENCY DOMAIN

In this section, we discuss the evolution of the history force $\tilde{F}_H$ in the frequency domain. For that purpose we introduce the normalized transfer function $\mathcal{F}$ defined as $\tilde{F}_H = 6\pi \mu_e R \tilde{W} \mathcal{F}$. The magnitude of the transfer function $\mathcal{F}$ obtained from our numerical simulations is compared in Fig. 10 with the Eqs. (14), (15), and (13) for a solid sphere, a spherical bubble, and a spherical fluid particle, respectively. The viscosity ratios $\mu^* = 0.05$, $\mu^* = 0.2$, and $\mu^* = 20$ are shown.

As observed, our numerical simulations are in very good agreement with the exact solution (13) for a fluid sphere over a wide range of viscosity ratio and oscillation frequency. At low frequency, $\mathcal{F}$ evolves as $\sqrt{f^*}$ in all cases. However, at high frequency, the transfer function for a spherical bubble tends to the value 4/3 while both our simulations and the exact relation (13) still evolve as $\sqrt{f^*}$. In
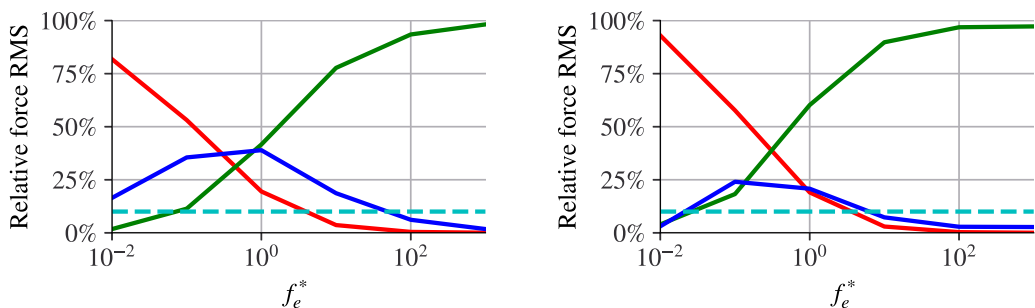

FIG. 9. Evolution of each force RMS relative to the total force RMS with f^*. —— Steady drag force RMS, —— Inertial (Pressure gradient) and added-mass forces RMS, —— History force RMS, - - - Limit 10% contribution. (Left) Simulation results with Re $= 0.01$ and $\mu^* = 5$. (Right) Simulation results with Re $= 0.1$ and $\mu^* = 0.05$.
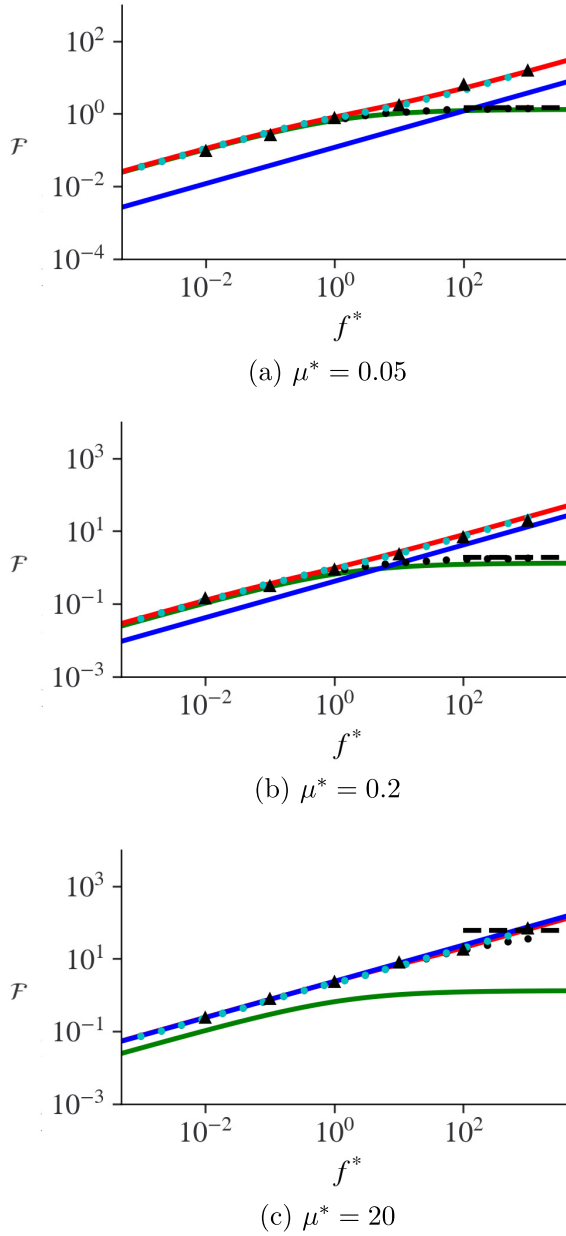
(a) $\mu^* = 0.05$

(b) $\mu^* = 0.2$

(c) $\mu^* = 20$

FIG. 10. Normalized transfer function $\mathcal{F} = \tilde{F}_h/6\pi\mu_e R\tilde{W}(f^*)$ as a function of f^* for different viscosity ratios: (a) $\mu^* = 0.05$, (b) $\mu^* = 0.2$, and (c) $\mu^* = 20$. ▲ Numerical simulations at Re $= 0.1$. —— Solid sphere (relation (14), —— Spherical bubble (relation (15)), —— Fluid particle of viscosity μ^* (relation (13)), ● relation (27) with slip length $\lambda = R/3\mu^*$ (relation (4)), ● relation (27) with unsteady slip length given by relation (24), and dashed line asymptotic value of our kernel when $f^* \to \infty$.

fact, much lower values for μ^* are required (typically lower than 10^{-3}) to be able to use the Yang and Leal history force relation at high frequency.
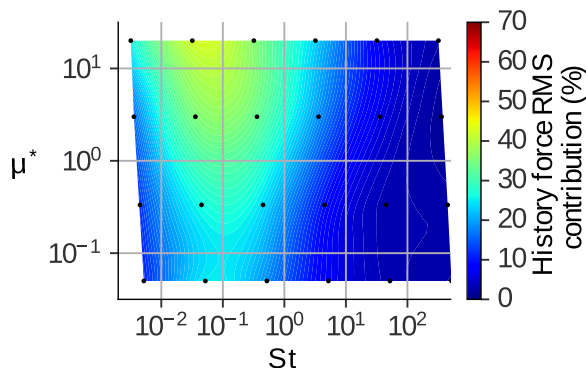
FIG. 11. Relative contribution of the history force RMS to the total force in the phase diagram St-μ^*. Color contours are created using Delaunay triangulation between our simulation data (black dots).

The transfer function of the history force Eq. (6) proposed by Legendre *et al.* [8] is reported in Fig. 10. The agreement is found to be very good at low frequency but a clear difference is observed at large frequency where Eq. (6) follows the behavior observed for a bubble. This result is consistent with the numerical simulations of Legendre *et al.* [8] that show that the the early time transient evolution of the slip length (corresponding to large values of f^*) can not be described by $\lambda = R/3\mu^*$ (relation 4). Legendre *et al.* [8] have proposed a correlation for the unsteady slip length which matches the numerical results

$$\lambda(\mu^*, t) = \frac{R}{3\mu^*}\left[1 - \exp\left(-\left(\frac{60\,t}{t_{vi}}\right)^{0.55}\right)\cos\left(\frac{20\,t}{t_{vi}}\right)\right], \tag{24}$$

where t_{vi} is based on the drop kinematic viscosity ν_i. As shown in Fig. 10, the evolution for large f^* is drastically improved when considering equation (24) instead of $\lambda = R/3\mu^*$ in the Kernel Eq. (6) and agrees very well with both the theoretical prediction and direct simulation results.

VII. KERNEL FOR HISTORY FORCE IN THE TIME DOMAIN

In the context of particulate turbulent flows, the dynamics of a dispersed phase made of droplets is usually characterized in terms of the Stokes number $\mathrm{St} = \tau_p/\tau_f$ that compares the droplet relaxation time τ_p to a relevant fluid flow timescale τ_f. If $\mathrm{St} \gg 1$, then the trajectory of the droplet is only weakly affected by the flow structures of characteristic time τ_f. Otherwise, if $\mathrm{St} \ll 1$, then the droplet evolves as a fluid tracer closely following the flow streamlines and can easily be captured by any vortex. In the intermediate regime of finite Stokes number, preferential accumulation is observed either within vortices for bubbles or in high strain regions for inertial solid particles. At small particle Reynolds number $\mathrm{Re} = \rho_e dW_0/\mu_e \ll 1$, τ_p is given by

$$\tau_p = \frac{2}{9}\frac{(\rho_i + C_M\rho_e)}{\mu^e}\frac{2 + 3\mu^*}{3 + 3\mu^*}R^2, \tag{25}$$

with C_M the added-mass coefficient equal to $1/2$ for a sphere. In the flow configuration considered here [see Eq. (7)], the flow timescale is the oscillation period $\tau_f = T$ and the Stokes number reads

$$\mathrm{St} = \frac{\tau_p}{T} = \frac{2}{9}(1 + \rho^*/2)\left(\frac{2 + 3\mu^*}{3 + 3\mu^*}\right)f^*. \tag{26}$$

Figure 11 shows the history force RMS reported in the phase diagram St-μ^* for St varying between 10^{-3} to 10^{+3} and μ^* between 0.05 and 20. The history force RMS contribution is found to be more than 10%, for Stokes number in the range $0.01 < \mathrm{St} < 5$. Similar results have been
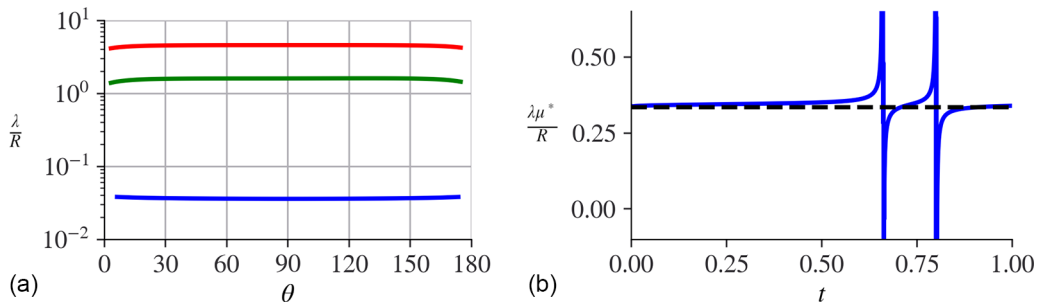
FIG. 12. (a) Interfacial slip length λ/R as a function of θ at $t = 0.25T$, for: —— Re = 0.1, $\mu^* = 0.2$, and $f^* = 0.01$, —— Re = 0.01, $\mu^* = 0.05$, and $f^* = 1$, —— Re = 0.1, $\mu^* = 5$, and $f^* = 10$. (b) Interfacial slip length λ/R as a function of time over a period, for Re = 0.1, $\mu^* = 0.2$, and $f^* = 0.01$.

observed for radial migration of particles in a vortex for St < 0.01 with a significant history force contribution [2]. At lower Stokes numbers, the history force RMS is almost equal to the steady drag RMS contribution, while at high frequency the pressure gradient and added-mass force are the dominant forces. However, the range of parameters (Stokes number and viscosity ratio) over which the history force must be considered is wide and corresponds to the regime where preferential accumulation is expected ($0.05 <$ St <5) for droplets ($0.5 < \mu^* < 10$). Therefore, an accurate expression for the history kernel able to calculate the unsteady force for Lagrangian tracking is highly desirable.

For that purpose, the expression of the history force,

$$F_H = 6\pi \mu_e R \int_0^t \frac{dW}{dt'} K_\lambda(t - t', \lambda) \, dt', \tag{27}$$

is computed using Simpson's method to guarantee second order accuracy. In the kernel expression given by Eq. (5), multiplications between exponential and complementary error functions can cause computational divergence because each term can easily overpass the maximum number of digits a computer can store, even if they compensate each over (the first one tends to infinity while the second one tends to zero). A solution to overcome this problem proposed by Daitche [5] is described in the Appendix, and used here for the computation of the history force.

The interfacial slip length is calculated by

$$\lambda = \frac{U_{\theta,e}}{r \frac{\partial}{\partial r} \left(\frac{U_{\theta,e}}{r} \right)}, \tag{28}$$

with $U_{\theta,e}$ the tangential velocity of the external fluid at the interface and r the radial position from the droplet center.

The interfacial slip length measured in the oscillatory flow considered here is reported as a function of the polar angle θ in Fig. 12(a). We can observe that the interfacial slip length 28 is uniform along the interface all over the oscillation period for the different cases considered, i.e., when varying both the viscosity ratio and the normalized frequency. We find a maximum deviation of λ along the interface of 1.5%, except when the flow changes direction because division by a zero shear stress occurs, see Fig. 12(b).

As Eq. (4) is relevant in most considered cases, it is introduced in Eq. (27) to calculate Eq. (5). The resulting history force is compared in Fig. 13 with direct numerical results for some reference cases. We observe a good agreement as long as $f^* \leqslant 100$. Otherwise, for $f^* > 100$ it appears that the model prediction is no longer in phase, and underestimates the amplitude of oscillation. The corresponding difference is quantitatively measured for all the cases with the mean absolute error
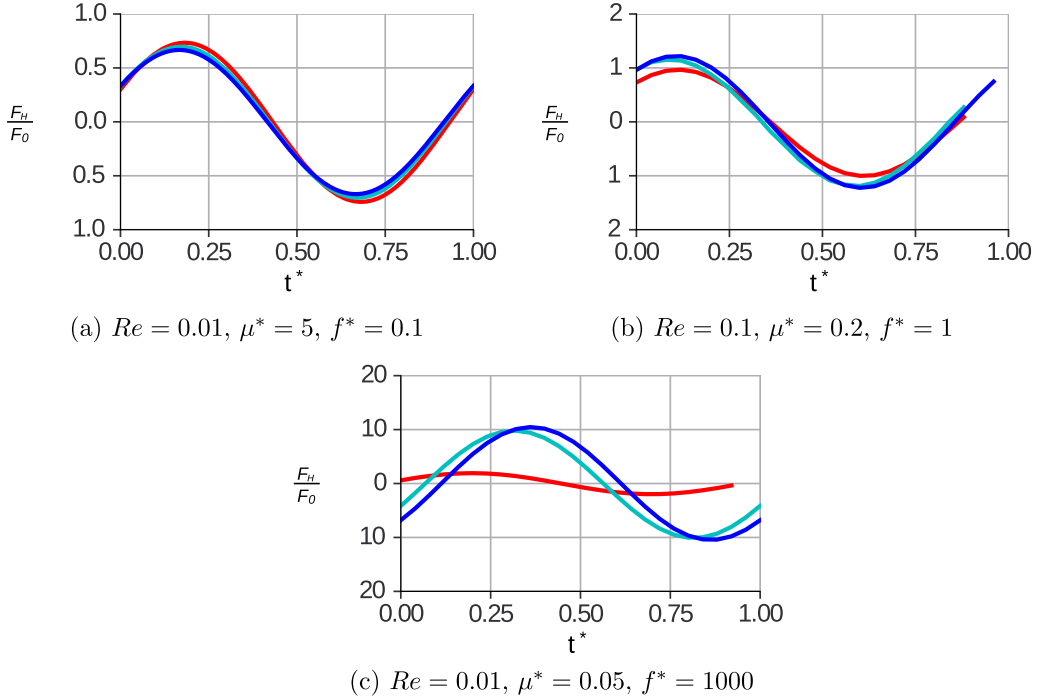
(a) $Re = 0.01$, $\mu^* = 5$, $f^* = 0.1$

(b) $Re = 0.1$, $\mu^* = 0.2$, $f^* = 1$

(c) $Re = 0.01$, $\mu^* = 0.05$, $f^* = 1000$

FIG. 13. Normalized history force as a function of the normalized time t/T. Comparison between direct simulations (——) and Eq. (5) (——) with the kernel given by Eq. (5), the slip length by relation (4) and (——) with the kernel given by Eq. (5) and the slip length by relation (24). (a) Re = 0.01, $\mu^* = 5$, $f^* = 0.1$ ($f_i^* = 0.02$), $r^2 = 0.9619$; (b) Re = 0.1, $\mu^* = 0.2$, $f^* = 1$ ($f_i^* = 5$), $r^2 = 0.9452$; (c) Re = 0.01, $\mu^* = 0.05$, $f^* = 100$ ($f_i^* = 2000$), $r^2 = 0.1970$.

(MAE):

$$\text{MAE}^*(F_{\text{H model}}, F_{\text{H}}) = \frac{1}{A(F_{\text{h}})n} \sum_{i=1}^{n} |F_{\text{H model}_i} - F_{\text{H}_i}|, \tag{29}$$

where n is the number of time steps.

The resulting difference map is shown in Fig. 14 (left). As expected, the difference between the model and the numerical simulations increases when increasing the Stokes number (i.e., the frequency f^*) for model with slip length Eq. (4), especially at low viscosity ratio. Using Eq. (24) for the slip length gives much better agreement with the simulation results at high frequency, see Figs. 10 and 15, over all the range of Stokes number and viscosity ratio. The discrepancy is only 4% at low viscosity ratio when the flow recirculation appears and develops more in the continuous phase. When comparing the plot in Fig. 14, to the plot reporting the relative contribution of the history force to the total force (see Fig. 11) we observe that the error in calculating the history force collapses to the region where its contribution to the total force is not relevant. Thus, the history force expression given by Eqs. (27) and (5) with slip length given by Eq. (4) is accurate when its contribution is of importance for the total force, as indicated by Fig. 14 (right). Interestingly, even if we cannot correctly predict the history force for some range of parameters, in those cases the history force contribution to the total force balance is negligible. As a consequence, the proposed history force expression given by Eqs. (27) and (5) with slip length (4) can be used for any set of parameters and will provide a significant improvement of droplet trajectory prediction when the history force contribution cannot be neglected. An even better accuracy can be achieved over the full range of
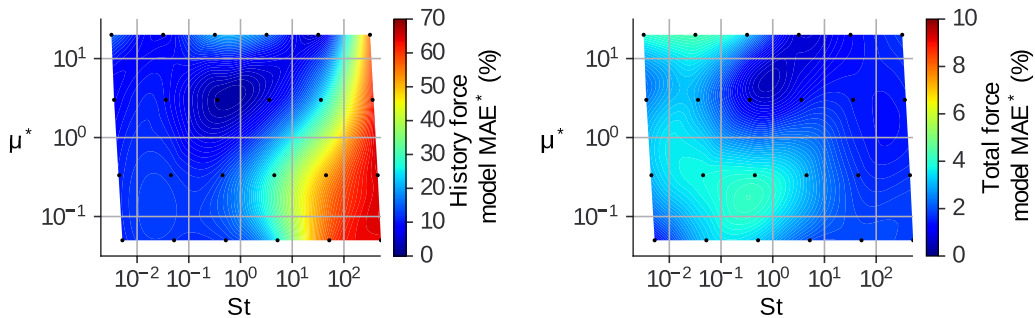
FIG. 14. Stokes and viscosity ratio map of (left) History force model MAE*, (right) Total force model MAE*, with slip length $\lambda = R/3\mu^*$ [Eq. (4)]. Contour is created using Delaunay [30] triangulation between data points.

physical parameters we investigated by using the history force kernel given by Eqs. (27) and (5) with an unsteady slip length (24).

VIII. CONCLUSION

Using direct numerical simulations, we have carried out a parametric study to characterize the history force acting on a droplet held fixed in an oscillatory uniform flow at low Reynolds number. To place such results in the context of turbulent dispersed two-phase flows, we analyzed our results in terms of the Stokes number and the viscosity ratio. Based on simulation results, the history force contribution found to be significant (typically larger than 10% of the RMS total contribution) for a wide range of Stokes number (typically between 0.5 and 5) and viscosity ratio (between 0.5 and 10) where all important dynamics of turbulence induced clustering is expected. Neglecting history force could lead to significant errors in the force balance, which makes it highly desirable to get an analytic history kernel for droplet trajectory equation.

Although an analytical expression of the history force kernel exists in the frequency domain, it cannot be transformed in the time domain for the general case of droplets (finite viscosity ratio). A model of the history force for droplets in the time domain has already been presented by Legendre *et al.* [8], and validated under creeping impulsive flow conditions. This model takes advantage of the analogy of the boundary condition existing at the drop interface and the slip length boundary condition for super-hydrophobic surface. We have tested this model, assuming a uniform and constant slip length at the interface in an oscillatory flow. We have obtained good agreement between the model and the DNS results for Stokes number below 10. It shows good agreement with
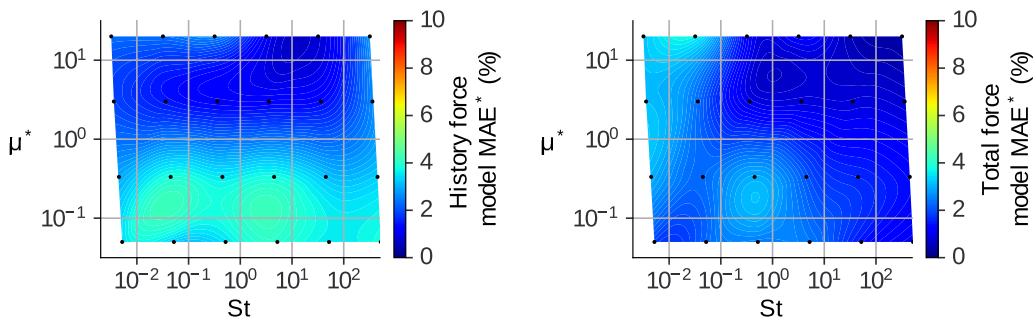

FIG. 15. Stokes and viscosity ratio map of (left) History force model MAE*, (right) Total force model MAE*, with slip length Eq. (24). Contour is created using Delaunay [30] triangulation between data points.

the analytical expression in the frequency domain for low to moderate frequency oscillations. Over a wide range of parameters relevant to most applications, we observe that the discrepancy between the history force model with constant slip and uniform slip length and the DNS results is small when the history force contribution is significant. Using a correlation fitted on simulation data to model the early time evolution of the slip length provides an even better accuracy over the whole frequency domain. Therefore, we propose a Basset-Boussinesq history force expression for droplets that can be used for any set of parameters, making possible an accurate calculation of droplet trajectory when the history force contribution cannot be neglected.

In addition, we report an appropriate method for the Kernel calculation, which allows easier computations and avoids overflow error from exponential and complementary error function terms.

APPENDIX: APPROXIMATION OF THE KERNEL TO AVOID OVERFLOW ERROR

History force has often been neglected due to the computational cost for the integration of the memory kernel in Eq. (5). For droplets, the problem is even worse because it involves multiplications between an exponential and a complementary error function. Indeed, each term can easily overpass the maximum number of digits a computer can store, even if they compensate each over (one tends to infinity when the other tends to zero). A solution is to approximate the complementary error function, with an exponential function with a negative power term, therefore compensating the exponential one: Abramowitz $et\ al.$ [31]. Considering the following function f:

$$f = e^y \times erfc(x), \tag{A1}$$

the numerical approximation of f consists in considering the following simplification of the complementary error function for $x > 1$ as

$$f = (a_1 b + a_2 b^2 + a_3 b^3 + a_4 b^4 + a_5 b^5) \times e^{y-x^2}, \tag{A2}$$

with

$$b = \frac{1}{1 + px},$$
$$a_1 = 0.254829592, \quad a_2 = -0.284496736,$$
$$a_3 = 1.42141741, \quad a_4 = -1.453152027,$$
$$a_5 = 1.061405429, \quad p = 0.3275911.$$

Considering now the expression of the memory kernel in Eq. (5), we see that the corresponding x and y of Eq. (A1) have a direct relation:

$$y = x^2,$$

that simplifies even more the expression of the memory kernel because we get rid of every exponential terms as shown in Eq. (A3) preventing overflow errors:

$$f = (a_1 b + a_2 b^2 + a_3 b^3 + a_4 b^4 + a_5 b^5). \tag{A3}$$

We show in Fig. 16, that the approximation, precisely, respects the exact solution.
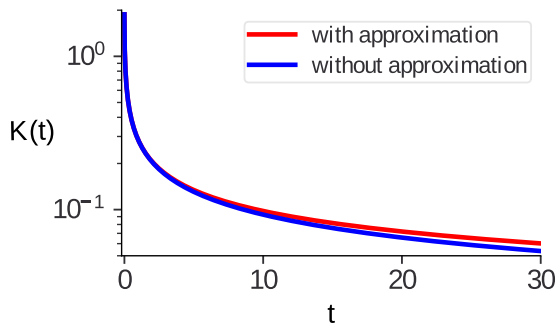
FIG. 16. Comparison of kernel computation with or without the approximation shown in Eq. (A3). The curve without approximation is computed using the python library mpmath to ensure accuracy and avoid overflow errors.

The expression of the history force with this simplification is then

$$F_h(t) = 6\pi\mu^e R \int_0^t \frac{dW}{dt'} a(a_1 b + a_2 b^2 + a_3 b^3 + a_4 b^4 + a_5 b^5)\, dt', \tag{A4}$$

with

$$a = \frac{(1 + 2\lambda/R)^2}{\lambda/R(1 + 3\lambda/R)} \quad \text{and} \quad b = \frac{1}{1 + p\left[\frac{(1+3\lambda/R)}{\lambda/R}\sqrt{t/t_\nu}\right]}.$$

If the analytic expression of $\frac{dW}{dt'}$ is known, then it is possible, in some cases, to integrate this expression exactly and get rid of the numerical integration. But calculating the history force in general cases needs to compute $\frac{dW}{dt'}$ along the trajectory. We cannot solve the integral exactly, but the reader can refer to the work of Daitche [5] for more details.

[1] S. Ravichandran, J. R. Picardo, S. S. Ray, and R. Govindarajan, *Fluid Dynamics in Clouds* (Springer, Berlin, 2020), pp. 1–23.

[2] F. Candelier, J. R. Angilella, and M. Souhar, On the effect of the Boussinesq-Basset force on the radial migration of a Stokes particle in a vortex, Phys. Fluids **16**, 1765 (2004).

[3] A. Daitche, On the role of the history force for inertial particles in turbulence, J. Fluid Mech. **782**, 567 (2015).

[4] G. Haller, Solving the inertial particle equation with memory, J. Fluid Mech. **874**, 1 (2019).

[5] A. Daitche, Advection of inertial particles in the presence of the history force: Higher-order numerical schemes, J. Comput. Phys. **254**, 93 (2013).

[6] E. E. Michaelides, Hydrodynamic force and heat/mass transfer from particles, bubbles, and drops—The Freeman scholar lecture, J. Fluids Eng. Trans. ASME **125**, 209 (2003).

[7] S. G. Prasath, V. Vasan, and R. Govindarajan, Accurate solution method for the Maxey-Riley equation and the effects of Basset history, J. Fluid Mech. **868**, 428 (2019).

[8] D. Legendre, A. Rachih, C. Souilliez, S. Charton, E. Climent, Basset-Boussinesq history force of a fluid sphere, Phys. Rev. Fluids **4**, 073603 (2019).

[9] M. J. Hadamard, Mouvement permanent lent d'une sphère liquide et visqueuse dans un liquide visqueux, Comptes rendus hebdomadaires des séances de l'Académie des Sciences **203**, 73 (1936).

[10] W. Rybczynski *et al.*, On the translatory motion of a fluid sphere in a viscous medium, Bull. Acad. Sci., Cracow, Series A **40**, 33 (1911).

[11] R. Gatignol, The faxen formula for a rigid particle in an unsteady nonuniform Stokes flow, Journal de mécanique théorique et appliquée **2**, 143 (1983).

[12] M. R. Maxey and J. J. Riley, Equation of motion for a small rigid sphere in a nonuniform flow, Phys. Fluids **26**, 883 (1983).

[13] A. B. Basset, On the motion of a sphere in a viscous liquid, Proc. Roy. Soc. London Series I **43**, 174 (1887).

[14] J. Boussinesq, Sur la resistance quoppose un liquide indefini en repos, sans pesanteur, au movement varie d'une shere solide, CR Acad. Sci. Paris **100**, 985 (1885).

[15] R. Mei, J. F. Klausner, and C. J. Lawrence, A note on the history force on a spherical bubble at finite Reynolds number, Phys. Fluids **6**, 418 (1994).

[16] S. M. Yang and L. G. Leal, A note on memory-integral contributions to the force on an accelerating spherical drop at low Reynolds number, Phys. Fluids A **3**, 1822 (1991).

[17] E. E. Michaelides and Z. G. Feng, The equation of motion of a small viscous sphere in an unsteady flow with interface slip, Int. J. Multiphase Flow **21**, 315 (1995).

[18] A. R. Premlata and H. H. Wei, The Basset problem with dynamic slip: Slip-induced memory effect and slip-stick transition, J. Fluid Mech. **866**, 431 (2019).

[19] V. A. Gorodtsov, Slow motions of a liquid drop in a viscous liquid, J. Appl. Mech. Tech. Phys. **16**, 865 (1976).

[20] S. Kim and S. J. Karrila, *Microhydrodynamics Principles and Selected Applications* (Butterworth-Heinemann, Boston 1991).

[21] C. Pozrikidis, A bibliographical note on the unsteady motion of a spherical drop at low Reynolds number, Phys. Fluids **6**, 3209 (1994).

[22] V. Galindo and G. Gerbeth, A note on the force on an accelerating spherical drop at low-Reynolds number, Phys. Fluids A **5**, 3290 (1993).

[23] M. Abbad and M. Souhar, Experimental investigation on the history force acting on oscillating fluid spheres at low Reynolds number, Phys. Fluids **16**, 3808 (2004).

[24] Z. G. Feng and E. E. Michaelides, Heat and mass transfer coefficients of viscous spheres, Int. J. Heat Mass Transf. **44**, 4445 (2001).

[25] A. Rachih, D. Legendre, E. Climent, and S. Charton, Numerical study of conjugate mass transfer from a spherical droplet at moderate Reynolds number, Int. J. Heat Mass Transf. **157**, 119958 (2020).

[26] D. Legendre and J. Magnaudet, The lift force on a spherical bubble in a viscous linear shear flow, J. Fluid Mech. **368**, 81 (1998).

[27] J. Magnaudet, M. Rivero, and J. Fabre, Accelerated flows past a rigid sphere, Part 1., J. Fluid Mech. **284**, 97 (1995).

[28] A. Rachih, Étude numérique du transfert de matière à travers l'interface d'une goutte sphérique en mouvement: Mise en évidence des effets 3d. Ph.D. thesis, Toulouse, INPT. (2019).

[29] E. J. Chang and M. R. Maxey, Unsteady flow about a sphere at low to moderate Reynolds number. Part 1. Oscillatory motion, J. Fluid Mech. **277**, 347 (1994).

[30] B. Delaunay *et al.*, Sur la sphere vide. Izv. Akad. Nauk SSSR, Otdelenie Matematicheskii i Estestvennyka Nauk **7**, 793 (1934).

[31] M. Abramowitz, I. A. Stegun, and R. H. Romer, *Handbook of Mathematical Functions with Formulas, Graphs, and Mathematical Tables* (Dover Publications, Mineola, NY, 1988).